Journal of Power Sources 517 (2022) 230715

Contents lists available at ScienceDirect

Journal of Power Sources

journal homepage: www.elsevier.com/locate/jpowsour

Electrocatalytic surface nanoionics with strained interfaced and colossal conductivity for enhancing durability and performance of solid oxide fuel cell

Yun Chen, Cesar O. Romo-De-La-Cruz, Sergio A. Paredes-Navia, Liang Liang, Alec Hinerman, Jacky Prucz, Mark Williams, Xueyan Song*

Department of Mechanical and Aerospace Engineering, West Virginia University, Morgantown, WV, 26506, USA

HIGHLIGHTS

- Conformal CoO_x nanoionics with discrete Pt nano-particles on LSCF/SDC.
- Heterogeneous CoO_x/Pt reduces the cell series resistance by 40%.
- CoO_x/Pt ALD layer possesses extraordinary nanostructure stability over 816 h.
- CoO_x/Pt ALD layer suppresses Sr outward diffusion.
- Conductivity of the ALD layer is two orders magnitude higher than that of LSCF.

ARTICLE INFO

Keywords:
Nanoionics
Solid oxide fuel cells
Atomic layer deposition
Sr surface segregation
Conductivity

ABSTRACT

For an oxygen electrode in solid oxide fuel cells (SOFCs) consisting of mixed electrical and ionic conducting lanthanum strontium cobalt ferrite (LSCF), it degrades due to its low chemical stability and cation surface segregation. To mitigate such degradation, for the first time in the field of SOFCs, we demonstrate a conformal ultra-thin (~10 nm) coating consisting of subjacent discrete nano-Pt capped with a superjacent conformal CoO_x layer, applied on LSCF/SDC composite electrode, using atomic layer deposition (ALD). The coating layer reduces the cell series resistance by up to 40%, presents extraordinary stability with an intact morphology after 816 h operation. The superjacent CoO_x surface nanoionics consists of randomly orientated but single-layered nano-grains, with high-density intergranular and surface grain boundaries serving as the electrochemical reaction sites and facilitating mass transport. The ALD coating turns the original perovskite surface that is vulnerable to cation segregation and degradation into an embedded strained interface phase with enormous conductivity. The coating layer appears to suppress Sr outward diffusion and confines a 2 nm Sr-enriched interface layer between the coating layer and the LSCF backbone. The conductivity of the coating layer is estimated to be $\sim 1.27 \times 10^4$ S/cm and two orders magnitude higher than that of LSCF.

1. Introduction

The rapid climate deterioration due to CO_2 emission and fossil fuel consumption has manifested the significance of technology developing for hydrogen that is an energy carrier with high energy density for versatile energy conversion with the minimum environmental impact. Solid oxide cells (SOCs) that can be powered by pure H_2 for electricity generation in the fuel cell mode and can work reversibly as an electrolyzer for H_2 production possess the unrivaled highest energy conversion efficiencies among all the competing technologies [1,2]. However, for stationary electricity generation with a long-term of 3–5 years, the current state-of-the-art solid oxide fuel cells (SOFCs) continuously face electrode degradation challenges. Developing more robust electrodes are still the top priority for SOCs development. In terms of the oxygen electrode, the current state-of-the-art high-performance electrode commonly employs a cobaltite-based perovskite, including lanthanum strontium cobalt ferrite (LSCF) [3]. LSCF has a high ionic and electrical conductivity, high oxygen self-diffusion coefficient, and oxygen surface

---

* Corresponding author.
E-mail address: xueyan.song@mail.wvu.edu (X. Song).

https://doi.org/10.1016/j.jpowsour.2021.230715
Received 5 September 2021; Received in revised form 24 October 2021; Accepted 29 October 2021

exchange coefficient. As an effective electrocatalyst, LSCF cathodes have active areas for oxygen reduction reaction across the entire surface.

Nevertheless, LSCF cathode presents inadequate long-term durability due to intrinsic materials degradation of Sr segregation [4–9]. For the SOFC stacks, electrode degradation caused by Sr surface segregation is further accelerated due to their interaction with the volatile Cr species that are evaporated from the Cr-containing interconnects. Although various solution-based infiltration has been developed to decorate the internal surface of the porous oxygen-electrode [10,11] its impact on enhancing the stability of the LSCF appears to be limited partially due to the discrete nature of the infiltrated materials with uncontrolled microstructure. To effectively mitigate the Sr surface segregation and Cr contamination, it is essential to have a conformal surface coating layer inert to both Sr and Cr and serving as the barrier for Sr outward diffusion and Cr inward diffusion. On the other aspect, completely sealing off the LSCF/SDC backbone surface leads to the loss of cathode electroactivity. So, such a coating layer must be capable of carrying sufficient electrocatalytic activity for the oxygen reduction reaction (ORR). Plus, this coating layer needs to possess sufficiently high ionic conductivity to facilitate subsequent mass transfer for the dissociated oxygen ions.

Other than the aforementioned strict requirement in terms of the chemistry, conformity, and electrochemical properties, the coating layer also needs to be applied to the internal surface of the porous electrode that possesses complex topography with a high aspect ratio. Furthermore, the nanostructured materials are thermally sensitive at a modest temperature of ∼400 °C [12,13] because of the large surface-to-volume ratio and high surface energy of nanocrystals. Accordingly, there is an enormous concern about the structural stability of nanocrystals in the coating layer at elevated temperatures for the desired lifetime. Therefore, developing a conformal coating to mitigate the Sr surface segregation in SOFCs, while maintaining the electrode's functionality is incredibly sophisticated.

Here we report a straightforward approach. We apply an ultra-thin nanocomposite consisting of Pt and CoO_x on the LSCF/SDC cathode backbone using Atomic Layer Deposition (ALD) [14]. This surface heterogeneous coating layer consists of subjacent discrete Pt nanoparticles capped with superjacent fully dense conformal CoO_x layer. The performance of the cells with this conformal ALD layer along with the baseline cells is examined and compared. Post-operation chemical and nanostructural examinations were carefully conducted. In particular, we studied the interface between the coating layer and backbone LSCF to reveal how this coating layer facilitates the performance and durability of the LSCF/SDC cathode SOFC.

2. Experimental section

Commercially available, anode-supported solid oxide button cells fabricated by Materials and Systems Research, Inc. (MSRI, Salt Lake City, UT) were employed for all the experiments described in this paper. MSRI cells are composed of five layers as follows, starting from the anode: a ∼700 μm thick Ni/YSZ cermet layer which supports the cell structure; a ∼10 μm thick Ni/YSZ active layer; a ∼10 μm thick YSZ electrolyte; a thin (2–3 μm), dense Sm_2O_3-doped CeO_2 (SDC) barrier layer, a ∼10 μm thick $La_{0.6}Sr_{0.4}Co_{0.2}Fe_{0.8}O_{3-\delta}$ (LSCF)/SDC active layer; and a 50 μm thick, pure LSCF current collecting layer. The active area (limited by the cathode) of the cell is 2 cm^2. The exposure area of the anode to fuel is about 3.5 cm^2.

The ALD coatings were performed in a commercial GEMStar-8 ALD reactor from Arradiance Inc. The precursors used in this study were all purchased from Strem Chemicals, Inc. The (trimethyl)methylcyclopentadienyl platinum(IV), (99%) and the deionized water were used as Pt precursor and oxidant for depositing Pt layer; and the bis (cyclopentadienyl)cobalt (II), (min. 98% cobaltocene) and ozone were used as Co and oxidant, respectively, for CoO_x layer growth. During the deposition, the (trimethyl)methylcyclopentadienyl platinum and bis (cyclopentadienyl)cobalt containers were maintained at 75 °C and 90 °C, respectively; and the reactor chamber was set at 300 °C. Desired cycles were performed for Pt and CoO_x deposition, respectively, leading to a dual-layer ALD coating of Pt first, followed by Co_3O_4 (120 cycles for both cells) on each cell cathode backbone. The Pt layer thickness (Pt loading level) is slightly different for the ALD coated cells. Cell no. 2 was processed 30 cycles, while cell no. 4 was processed 60 cycles and had the loading of Pt twice as cell no. 2. No masking or specific treatment is applied on the NiO/YSZ anode before ALD processing. The thick and very dense NiO/YSZ anode prevents precursor penetration during the ALD processing, and the impact of ALD coating on the Ni/YSZ anode is negligible. No surface pretreatment or heat-treatment was applied before or after ALD coating either. The cell electrochemical operation was carried out directly after the ALD coating.

One baseline cell no. 1 and ALD coated cell no. 2 was subject to operation at 750 °C, and the other baseline cell no. 3 and the coated cell no. 4 were examined at 650 °C. All cell tests were performed on a test stand. The platinum mesh was used for anode and cathode lead connections. The fuel and air stream flow rates were controlled separately using mass flow controllers. During the operation, a 400 mL/min air flow rate and a 400 mL/min fuel flow rate were used. Before any electrochemical measurements, both cells were current-treated for approximately ∼15 h under a small current density of 0.1 A/cm^2 to ensure they were activated. After that, the samples were loaded at a constant current of 0.3 A/cm^2 for desired periods. The cell performance was examined using a TrueData-Load Modular Electronic DC Load, which guarantees voltage and current accuracies of 0.03% FS of the range selected ±0.05% of the value. The cell impedance spectra were examined using a potentiostat/galvanostat (Solartron 1287A) equipped with a frequency response analyzer (Solartron 1260). Impedance measurements were carried out using a Solatron 1260 frequency response analyzer in a frequency range from 50 mHz to 100 KHz. The impedance spectra and resistance (ohmic resistance R_s and polarization resistance R_p) presented are those measured under a DC bias current of 0.3 A/cm^2. On a Nyquist plot, R_s is determined by the intercept at the higher frequency end, and R_p is determined by the distance between two intercepts.

After the electrochemical operation, the ALD coated cells were sectioned and subjected to nanostructural and crystallographic examination using high resolution (HR) Transmission Electron Microscopy (TEM). TEM samples were prepared by mechanical polishing and ion milling in a liquid-nitrogen-cooled holder. Electron diffraction, diffraction contrast, and HRTEM imaging were performed using a JEM-2100 operated at 200 kV. All the TEM examinations were conducted in the cathode active layer. Chemical analysis was carried out under TEM using energy dispersive X-ray Spectroscopy (EDS). High-angle annular dark-field (HAADF) Z-contrast imaging and nanoscale chemistry analysis were performed using an Aberration-Corrected 200 kV(JEOL 2100F) STEM with the inner cut-off angle of the HAADF detector set at >52 mrad.

3. Results and discussions

3.1. Conformal single-layered nanograins on LSCF/SDC cathode at 750 °C

As shown in Fig. 1, upon the electrochemical operation at 750 °C for 24 h, the baseline cell no. 1 possesses a peak power density of 0.949 W/cm^2 at 1.7 A/cm^2, with an R_s value of 0.112 Ω cm^2 and Rp of 0.238 Ω cm^2. For ALD coated cell no. 2, the peak power density reaches 1.273 W/cm^2 at 0 h, and 134% over the baseline. The power density increase is accompanied by the reduction of R_s to 0.068 Ω cm^2 by 39%, while the R_p for cell no. 2 is 0.274 Ω cm^2 and slightly higher than the baseline cell. As listed in Table 1, R_s increases to 0.084 Ω cm^2 after operation for 96 h. After that, R_s has little change from 96 h to 502 h while the R_p gradually increases. Due to the considerable reduction in the R_s, the peak power density of ALD coated Cell after 502 h operation remained to be 119% of that baseline cell at 24 h operation.

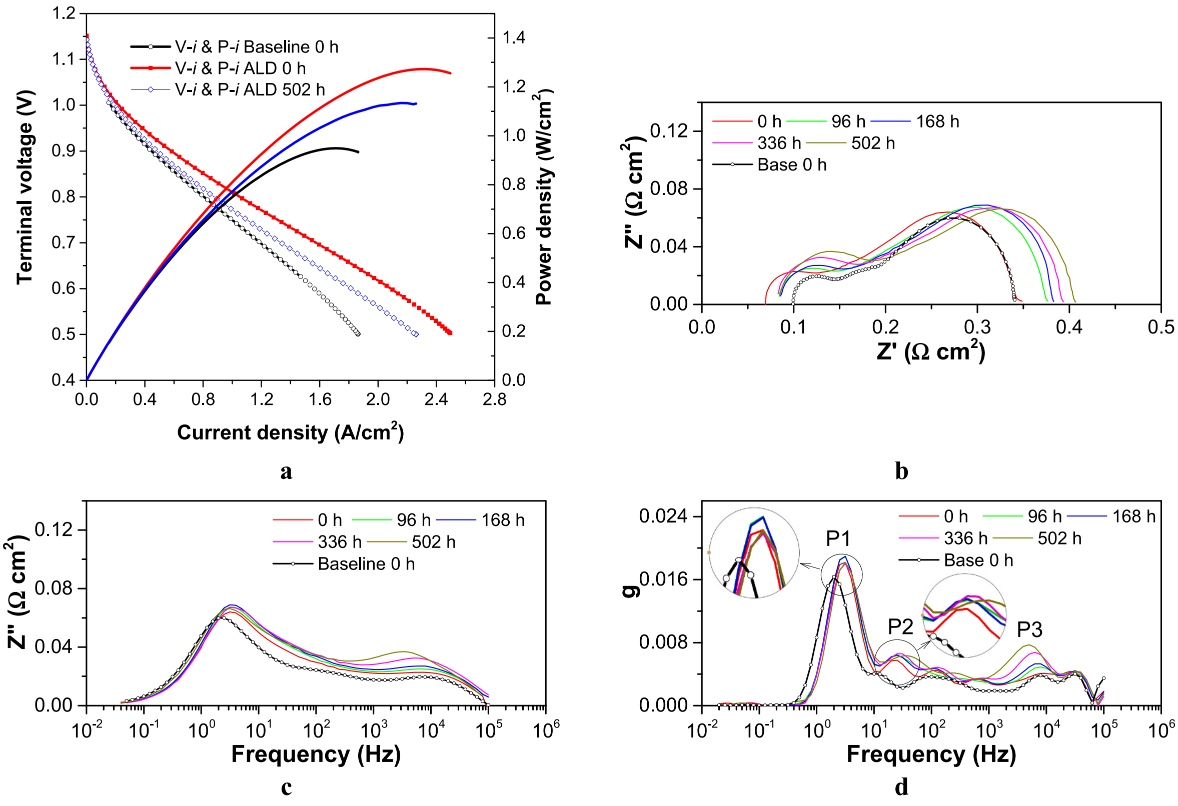

Fig. 1. Power density and impedance for the baseline cell no. 1, cell no. 2 LSCF cathode backbone with 2 nm Pt layer plus 10 nm CoOx. **a.** Terminal voltage as a function of current density for the cells at 750 °C. **b.** Nyquist plots of four cells at 0.3 A/cm^2. **c.** Bode plots of cells at 0.3 A/cm^2. **d.** Corresponding deconvolution spectra of the impedance data collected from two cells.

Table 1
Impedance and peak power density of the baseline cell no. 1 and cell no. 2 with 2 nm Pt layer plus 10 nm CoO$_x$.

LSCF/SDC cathode	Operating time (h)	R_s (Ω cm^2)	R_p (Ω cm^2)	Peak power (W/cm^2)	Enhancement to cell no.1 at 24 h
Baseline cell no. 1	24	0.112	0.237	0.949	/
Pt&CoO$_x$ coated cell no. 2	0	0.068	0.274	1.273	1.34
	96	0.084	0.291	–	1.19
	168	0.086	0.297	–	–
	336	0.082	0.311	–	–
	502	0.085	0.32	1.134	1.19

To identify the physical origin of cell performance enhancement and the slightly increased polarization resistance, the dynamic constant in the impedance data is retrieved by evaluating the relaxation times and relaxation amplitude of the impedance-related processes using deconvolution [15–18] shown in Fig. 1d. The cells exhibit one dominant arc P1 accompanied by P2 with lower magnitude, with the frequency ranging at 2–4 Hz, 20–40 Hz, respectively. The P1 and P2 arcs of the ALD coated cell no. 2 shift to the higher frequency end in comparison with that of the baseline. In general, for the cathode, the physical processes occurring at the characteristic frequencies of 5–150 Hz range could be assigned to activation polarization ORR. Depending on the cathode chemistry, the peaks could shift slightly to either direction under the identical cell operation conditions [15,19,20]. In comparison to the baseline cell no. 1, ALD coated cell no. 2 depicted higher amplitude P2 at ~20–40 Hz. It is recognized in the literature that the physical origin of the P2 arcs that arise at ~70 Hz is primarily due to oxygen transport along the surface and/or through the bulk in the cathode and electrolyte [18]. Thus, ALD coating of a Pt-CoO$_x$ dual layer on the surface of LSCF/SDC cathode has changed the cathode reaction pathways and introduced two apparently different cathodic polarizations. Each of the polarizations probably has its distinct dissociative oxygen adsorption and transport of oxygen species to the electrochemically active sites. For the ALD coated cell no. 2, P2 slightly increases during operation. However, P1 continuously decreased, implying the slightly, but continuously, accelerated ORR and oxygen transport upon operation.

The operation also introduced an increase in the P3 peak in cell no. 2 at high-frequency range 4752–9000 Hz. It is discussed in the literature that the Peak P3 could be associated with the charge transfer across the electrode/electrolyte interface, which is independent of the oxygen partial pressure [21]. So P3 is expected to be present in both the ALD coated cell and the baseline cell. The increase of P3 could be related to the formation of insulating phases in the cathode. For example, one possibility is the formation of a SrZrO$_3$ phase that inevitably takes place at the interface between the SDC barrier layer and the LSCF due to the solubility of Sr in the barrier layer phase. This is beyond the scope of this work that is focusing on the surface modification of the porous electrode.

Based on the impedance deconvolution, the subsequent equivalent circuit fitting and the capacitance analysis was performed. Cell no. 2 has lower chemical capacitance than cell no. 1, implying less involvement of the cathode backbone through the oxygen reduction reactions and related mass and charger transfer [22]. Furthermore, the ALD coated cell has continuous reduction of chemical capacitance with the increase of operation (shown in supplementary data), revealing the continuously increased surface transport and reactions in the overall electrode reaction in the ALD coated cell.

Overall, the ALD coated cell exhibits slightly higher R_p for both ORR and oxygen transport. The increased power density is attributed to the decreased R_s, implying the ALD coating has introduced additional mass or charge transfer pathways. Post-mortem nanostructural examination indicates that the ALD layer is of ~10 nm thick and remains to be fully conformal, dense, and uniform (in Fig. 2 a and b). The conformal coating consists of single-layered CoO_x grains (7–10 nm in dimension), capping the subjacent layer of discrete elongated Pt (~2 × 5 nm in size) nanograins that are ~ 20 nm apart. The single-layered CoO_x grains with random orientations has a very high density of intergranular and surface grain boundaries. The chemistry of the ALD layer is close to $Co_{0.9}Fe_{0.1}O_x$ with a small amount of Fe diffusion from LSCF, while it is free of Sr and La. As a consequence, this dense conformal CoO_x coating should have suppressed the Sr further surface segregation. Accordingly, we believe such a CoO_x layer could also act as a blocking layer to prevent the attack from other common contaminants in the SOFC system. One example is that Cr deposition occurs preferentially on the segregated SrO but not on Co_3O_4 [23], and the dense Co_3O_4 layer could separate the Cr vapor from its reaction with Sr cation [24]. Another example is such a dense coating layer could prevent the penetration of humidity into the cathode backbone that could also cause significant performance degradation [25]. In short, a significant increased intrinsic durability and contamination tolerance is expected due to the conformal ALD coating.

Underneath the superjacent layer, an ultra-thin layer is confined at the interface between CoO_x and the LSCF bulk phase (in Fig. 2). As shown in the STEM image in Fig. 2 c, this interface layer shows a brighter contrast, revealing the segregation of the atoms with heavier atomic numbers. TEM/EDS analysis (the electron beam sampling size ~ 20 nm) was conducted and showed that the typical La/Sr ratio for the intragranular LSCF grains is 6/4 as expected for the LSCF phase. By contrast, in the CoO_x/bulk LSCF interface region, the La/Sr ratio is 4/6. We could conclude that Sr is enriched in this interface layer. The atomic resolution Z-contrast (Fig. 2d) taken from [100] direction of the LSCF revealed that the La/Sr lattice arrangement of this Sr enriched layer is not different from that of the bulk LSCF. However, the Fe/Co column in the Sr-enriched layer depicts higher intensity than that in the LSCF bulk grains. Brighter contrast of atom columns implies the substitution of heavier elements (in this case Sr) in the Fe/Co sites. The multi-slice simulation was performed accordingly and confirmed that, when 50% of Fe or Co are substituted by Sr, the Fe/Co atomic columns present the increased intensity, as shown in Fig. 3. In other words, the chemistry of the Sr enriched layer is determined as $(La_{0.6}Sr_{0.4})(Co_{0.1}Fe_{0.4}Sr_{0.5})O_x$.

3.2. *Conformal superjacent single-layered nanograins on LSCF/SDC cathode at 650 °C*

The increased conductivity induced by the ALD layer appears to be tunable by adjusting the loading of the Pt. Cell no. 4 has a Pt loading that is doubled compared to cell no. 2. For cell no. 4 operated at 650 °C, the initial peak power density is 0.578 W/cm^2 at 0 h, and 125% over the baseline cell no. 3 of 0.463 W/cm^2 (shown in Fig. 4). R_s and R_p are 0.163 $\Omega\ cm^2$ and 0.454 $\Omega\ cm^2$ for cell no. 4 and 0.247 $\Omega\ cm^2$ and 0.442 $\Omega\ cm^2$ for cell no. 3, respectively. The impedance indicates a substantial reduction is reached for R_s, and the reduction is 34% compared to baseline cell no. 3. After operation for 816 h, cell no. 4 still exhibits a peak power density of 0.533 W/cm^2, and R_s and R_p are 0.168 $\Omega\ cm^2$ and 0.479 $\Omega\ cm^2$, which is 92% of its initial power density.

Deconvolution study indicates that, the peak of P1 of baseline cell no. 3 is close to that of P1 from cell no. 1 operated at 750 °C. However, there is a large increase in the P2 in the cell no. 4. This could be attributed to the increased resistance of O_2 transport when the operating temperature is lowered from 750 °C to 650 °C. The P1 from the ALD coated cell no. 4 is higher than the baseline cell no. 3, implying a slightly higher ORR resistance after coating. However, the P2 for cell no. 4 is much lower, revealing the much accelerated oxygen transport along the surface with the coating layer. Remarkably, for cell no. 4, both P1 and P2 remained at their same positions, implying the surface layer is very stable upon the electrochemical reactions for over 800 h. Furthermore, both P1 and P2 considerably decreased, showing slight but continuous improvement of the oxygen surface exchange, oxygen adsorption/desorption, dissociation, and/or surface transport. As shown in the supplementary data, there is decreased chemical capacitance, consistently revealing the possible less involvement of the cathode bulk in the overall electrode reaction in the ALD coated cell.

Post-mortem nanostructural examination indicates that the ALD layer remains intact and has the same morphology of that as-deposited state and is conformal on both the LSCF and SDC grain surfaces after operation for 816 h (shown in Fig. 5).

3.3. *Coating altered the oxygen reduction reactions pathways and accelerated mass-transfer through surface nanoionics via the strained interface*

Based on the results of both cells no. 2 and 4, we propose the ORR pathways and the schematics for possible surface nanoionics of LSCF cathode, as shown in Fig. 6. For the baseline cathode, the ORR takes place on the surface of LSCF. For the ALD coated cells, the conformal and dense ALD film is less permeable to oxygen and thus possibly reduces the activity of LSCF serving as the ORR sites. Instead, the surface nanograined CoO_x phase becomes the oxygen reduction sites. Electrocatalytic CoO_x covers both the LSCF and SDC phases and provides two distinguishable ORR sites that are also evidenced by the P1 and P2 peaks in impedance deconvolution (Fig. 1d). Though the nano-grained CoO_x shows inferior catalytic activity comparing to that of the LSCF, the

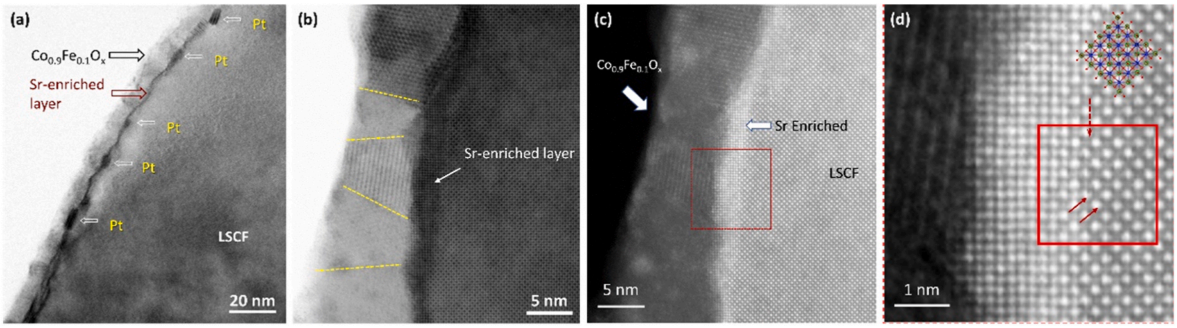

Fig. 2. TEM of cell no. 2 (Pt and CoO_x on cathode backbone) after operation at 750 °C for 502 h. **a.** A conformal dense $Co_{0.9}Fe_{0.1}O_x$ film covering the discrete Pt particles. There is Sr enriched interface phase between $Co_{0.9}Fe_{0.1}O_x$ film and the LSCF backbone. **b.** STEM bright field imaging depicting the $Co_{0.9}Fe_{0.1}O_x$ is single layered nano-grains with high density intergranular grain boundaries and surface grain boundaries. The Sr enriched layer is ~2 nm thick. **c.** STEM dark field imaging is taken from the [100] direction of LSCF. Sr enriched layer is shown at the interface (brighter contrast indicating the enrichment of heavy element). **d.** The enlarged box area in c showing the region of the interface between the Sr-enriched phase and the LSCF grain as indicated by the dashed arrow. The Sr enriched interface is fully epitaxial and coherent with the LSCF grain, presenting the same atom arrangement of that LSCF grain. The Sr-enriched interface shares the same La/Sr site column intensity of LSCF. However, the Co/Fe site column intensity is much stronger than that of LSCF.

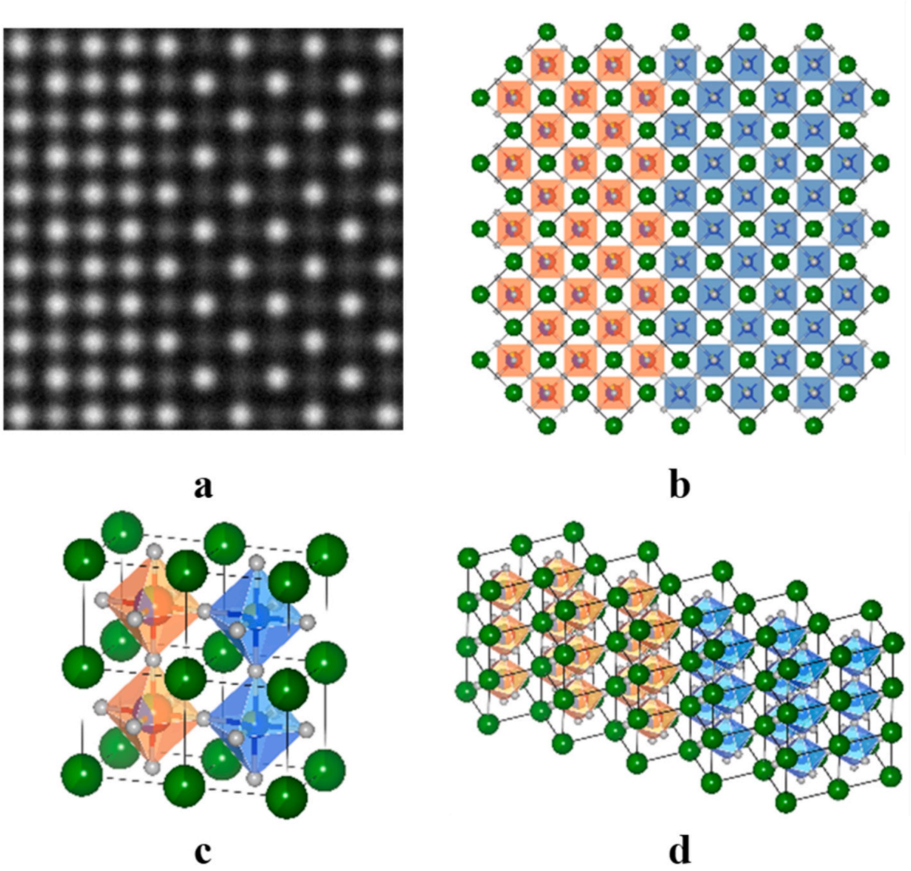

Fig. 3. **a.** Simulated STEM dark field imaging from the box area in the box area in Fig. 2d **b.** Atom arrangement of simulated area in Fig. 3 a. In the Sr enriched region, the La/Sr columns are the same as that of LSCF grain. However, 50% of Co/Fe atom columns are substituted by Sr. **c.** The atomic structure at the interface between the Sr-enriched interface phase and the LSCF, depicting the larger ionic size of Co/Fe site in the Sr enriched phase. **d.** 3D structure of the interface region.

increased active sites on SDC surfaces may partially compensate for the loss of the LSCF catalytic activity.

Since the CoO_x layer is fully dense and has low oxygen permeability, it is probable that Pt has the effective pathway to access oxygen. We think Pt at the interface primarily facilitates the formation of the CoO_x layer and further stabilizes this layer over the operation. Without the Pt, an ALD coating of unary CoO_x does not form a conformal CoO_x layer on either LSCF or SDC grains [26]. Here discrete nano-Pt is immiscible with its neighboring CoO_x and LSCF phases. On the other hand, nano-Pt may provide the interface strain to stabilize the formation of the conformal nanoionics [27,28]. It is worthwhile to point out the higher Pt loading in cell no. 4 does not promote the conductivity. The CoO_x + Pt coating layer in cell no. 4 only reduces 34% R_s over the baseline cell, while the reduction of R_s is 39% for cell no. 2 with only half Pt loading. In other words, the nano-Pt at the interface between CoO_x phase and LSCF phase might have negative impact to the cathode conductivity. It is reported that the difference in the Fermi level can result in the occurrence of electronic/ionic charge redistribution for the oxide surrounding the Pt particles [29]. Pt changed the oxide with which it is in contact into a resistance phase, resulting in the formation of a resistive oxide layer on the surface of Pt. Therefore, it is critical to control the maximum loading of dispersed Pt embedded at an interface to facilitate the percolation network and avoid the formation of a continuous resistance layer around Pt.

Overall, the ORR pathways could be shifted from the original LSCF surface to the CoO_x surface in the coated cells. Though the more active LSCF surface is covered, a full extension of the CoO_x active sites to the entire backbone surface is obtained. Also, the dissociated oxygen ions can only transport via the CoO_x intergranular grain boundaries due to the existence of a fully dense CoO_x outer shell layer.

Besides acting as catalytic oxygen reduction sites, the single 7–10 nm CoO_x layer apparently carries sufficient conductivity. The bulk scale Co_3O_4 phase is an amphoteric semiconductor with intragranular low electronic conductivity (~2 S cm^{-1} at 600 °C) [30], and is two orders of magnitude lower than bulk LSCF (~100 S cm^{-1} at 600 °C). However, a 133–134% cell performance enhancement is primarily attributed to the decreased R_s [3]. Our explanation is that, an increased conductivity induced by the conformal CoO_x layer is facilitated by the fast ion transport through the high-density, high-density grain boundaries, including the surface grain boundaries from the single-layered CoO_x nanograins [31–36]. In general, the high series resistance in the oxygen electrode is due to the low mobility of the ionic charge carriers and their mechanical and coulombic interactions with their host crystal structures [34]. By contrast, in comparison with the intragrain conductivity, there is faster oxide-ionic conductivity along grain boundaries that are commonly associated with higher oxygen vacancy concentration. One example is that $La_{0.8}Sr_{0.2}MnO_3$ (LSM) grain boundaries exhibits 5-6 orders of magnitude of enhancement in oxide-ion diffusivity compared with the bulk LSM. The enhancement might be associated with strain-induced defects and corresponding changes in the oxidation states of LSM constituent cations [30,34,37]. Dominating of ionic conductivity at the grain boundary level was also reported for $La_{0.6}Sr_{0.4}CoO_3$ [38,39]. In terms of high ionic conductivity of Co-based nanograins, we have demonstrated the formation of $(MnCo)O_x$ nanoionics implanted on the surface pure electronic conductor LSM in our previous study [40]. However, for the mixed conducting LSCF/SDC backbone, to the best of our knowledge, the present study is the first demonstration of electrocatalytic surface nanoionics that are implanted on the surface of the inherently functional SOFC. Such surface nanoionics immediately lead to the nanostructured electrode that has been pursued for decades for

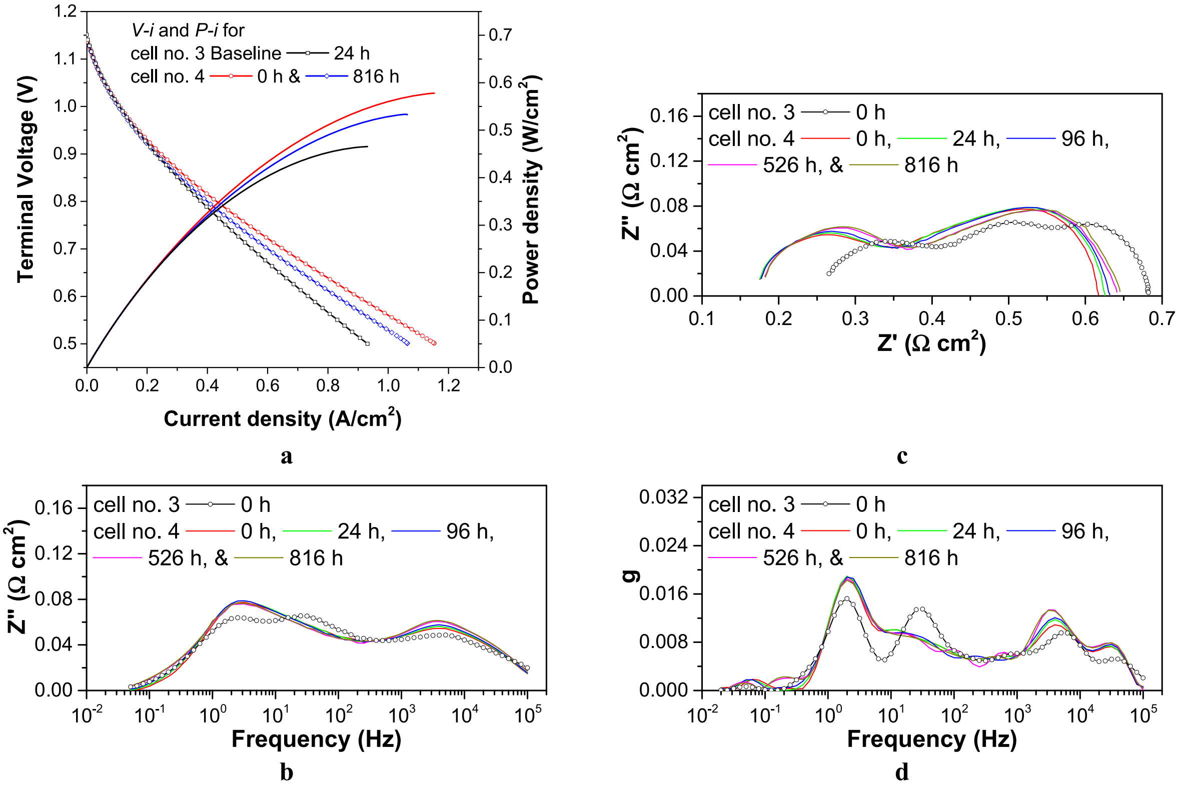

Fig. 4. Power density and impedance for the baseline cell no. 3 and cell no. 4 LSCF cathode backbone with 2 nm Pt layer plus 10 nm CoO_x. **a**. Terminal voltage as a function of current density for the cells at 650 °C. **b**. Nyquist plots of four cells at 0.3 A/cm^2. **c**. Bode plots of cells at 0.3 A/cm^2. **d**. Corresponding deconvolution spectra of the impedance data collected from two cells.

practical SOFC.

In addition, to facilitate the formation of nanoionics and prevent Sr surface segregation, the ALD coating further tuned the conductivity through the simultaneously formed Sr enriched interface layer. The impact of this Sr-enriched layer on the conductivity of LSCF grain is two-fold. Firstly, for the Sr-enriched layer alone, when Sr^{2+} is replacing Fe or Co cations with a higher valence state, it causes a decrease in the charge carrier concentration and leads to a lower electrical conductivity. Meanwhile, there is a small amount of Co cations substituted for the Fe in the Sr enriched layer, evidenced by the presence of a small amount of Fe cation inside the CoO_x coating layer. For the perovskite LSCF, Co ions on the Co/Fe sites have a smaller binding energy for oxygen than that with Fe ions [3,41]. Increasing the Co content could increase the electrical conductivity. Accordingly, the decreased electrical conductivity due to Sr enrichment could be compensated by Co substitution of Fe. Meanwhile, when a stable valent cation (Sr^{+2}) replaces a multivalent cation (oxidation state +3 and + 4) in the system, the charge compensation of B-site cation is achieved by the development of oxygen-deficient nonstoichiometry [42]. It is believed that the Sr enriched layer has high oxygen vacancy and possesses high ionic conductivity.

Secondly, the Sr-enriched layer imposes the strain field at its lateral interface with the LSCF grain surface. The Sr enriched layer possesses the same perovskite structure of that LSCF, shares the same kind of atomic structure in the La/Sr site, and is fully coherent to the LSCF grain as shown in Fig. 3 d. However, due to the larger ionic size of Sr ions in comparison with Co and Fe, the Sr enriched layer presumably has a larger lattice parameter than that of the LSCF grain as schematized in Fig. 3 c. This Sr-enriched layer spontaneously imposes the tensile strain on the LSCF grain surface. Such tensile strain increases the interatomic distance and weakens the atomic bonding strength on the surface layer of LSCF grains. Therefore, oxygen vacancies and ionic conductivity increase accordingly.

Such analysis of the impact of the strain field effect of ionic conductivity is consistent with the literature reports. At the interface of laterally aligned heteroepitaxial YSZ film grown on $SrTiO_3$ substrate, a huge, up to eight order of magnitudes enhancement conductivity was observed near room temperature [43]. Such a huge increase of conductivity was ascribed to the lattice expansion of atomic layers of YSZ phase elongated by the $SrTiO_3$ substrate with 7.5% tensile strain. For LSM, it was predicted by Density Function Theory calculation that tensile strain could improve ion diffusion up to 2 orders of magnitude at 800 K by increasing the migration space of oxygen in the lattice and by reducing the bonding strength between the oxygen and cations [44]. Such an increase of the conductivity of the strained interface are usually achieved in various nanocomposite grown by pulsed laser deposition [45,46]. Nonetheless, that substrate-strained engineered interface usually needs to be introduced by the epitaxial growth on the substrate with a well-defined orientation. The implantation of such strained interface in the real electrochemical devices with randomly orientated grains has been found to be typically limited. So far, there is no realization of the strained multi-layer on the SOFC electrode that needs the enhanced interfaces and grain boundaries for increased catalytic activity and conductivity [47–49].

In this study, planar strained lattices are generated spontaneously between the LSCF and Sr enriched layer that is fully coherent to the LSCF. The strained pathways formed at the interface between the ALD layer and the LSCF, are fully conformal. Once again, when the ALD coated layer with the strained interface was applied to the internal surface of the cathode, it remarkably decreases the entire cell R_s by up to 40%. Factor in the thickness of ALD layer of 10 nm on the internal surface of cathode with micron-sized grains, and taking the cell resistance as the contribution of cathode, anode, and electrolyte, we roughly estimated the conductivity of the ALD layer, as detailed in the supplementary document. At 750 °C, the conductivity of the ALD layer with the total thickness around ~10 nm, with the combination of conformal CoO_x

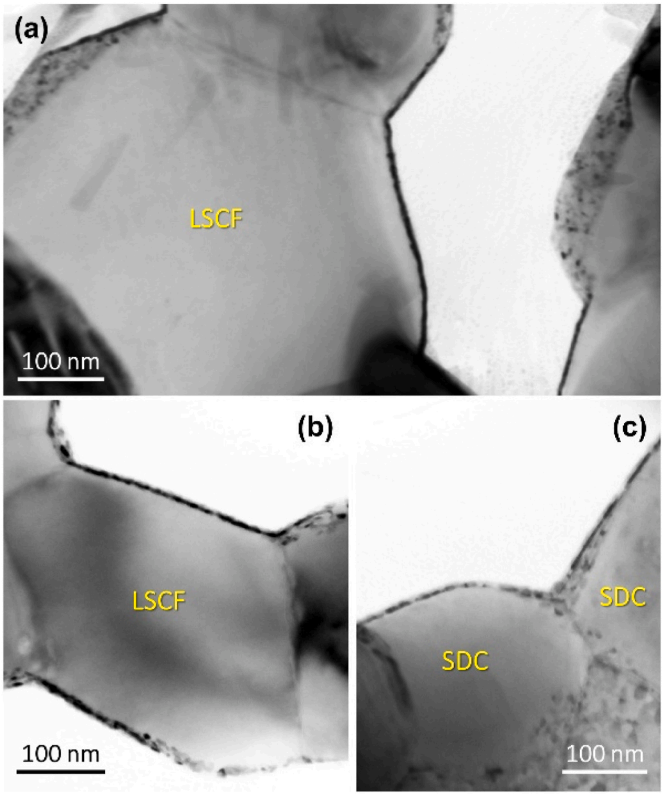

Fig. 5. TEM images showing as-deposited Pt + CoO_x coating layer and the layer after operation for 816 h at 650 °C. **a.** As-deposited conformal fully dense ALD coating layer. **b.** Conformal ALD film on LSCF backbone after operation for 816 h. **c.** Conformal ALD layer on SDC backbone after operation for 816 h.

layer, Sr enriched layer, and the strained interface, is estimated to have a conductivity of $\sim 1.27 \times 10^4$ S/cm, which is approximately two orders magnitude of that of LSCF at 750 °C.

Most importantly, such surface nanoionics are remarkably stable as evidenced by the intact nanostructure of the coating layer even after 816 h of operation at 650 °C, as shown in Fig. 5. Such stable nanostructure morphology is entirely consistent with the electrochemical performance. In cell no. 4, there is continuous accelerated transport of oxygen species and continuously reduced oxygen transport resistance upon operation. The increased conductivity is presumably partly due to the minimal amount of Fe incorporation into the CoO_x layer during the operation. Most importantly, the CoO_x conformal coating that also facilitated the Sr enriched layer at its strained interface could be continuous, and contributing to the increased conductivity.

The present study validated the previous research in the enhanced ionic conductivity due to the strained interfaces between different materials. With superior stability at elevated temperatures, the ultra-thin electrocatalytic surface nanoionics and its associated Sr enriched strained interface phase have become interfaces-dominated for maximized mass transport and oxygen reduction reactions. Such ALD coating appears to be the most promising approach to conveniently utilizing the grain boundary and strain engineering to increase the reaction kinetics of inherent functional devices.

4. Conclusion

The ability to manipulate the surface chemistry of the mixed conductor and suppress its degradation related to the intrinsic Sr surface segregation is critical for the SOFCs. The present work demonstrates that, for the inherent functional SOFC with a mixed conducting composite cathode, the electrocatalytic nanoionics with high-density grain boundaries could be precisely introduced onto the cathode backbone. The conformal thin-film surface nanoionics can be controlled to have the single-layered, randomly orientated nanograins to maximize the contribution of surface grain boundaries and the interface strains to the conductivity and the electrocatalytic activities. The conformal ALD layer completely shifted the ORR reduction pathways. It also serves as the effective barrier layer for backbone cations outward diffusion.

Most importantly, the ALD coating turns the original perovskite surface that is vulnerable to cation segregation and degradation into an embedded strained interface phase with enormous conductivity. For the first time in the field of SOFC, our study demonstrates an effective approach for solving multiple-problems for successfully suppressing the Sr surface segregation of mixed conductors, preventing Cr contamination, and simultaneously increasing the conductivity. The high-density surface and intergranular grain boundaries of the strained ALD layer provide an enormous surface area and interface area for facilitating multiple mass transport and catalytic reactions. It opens new research

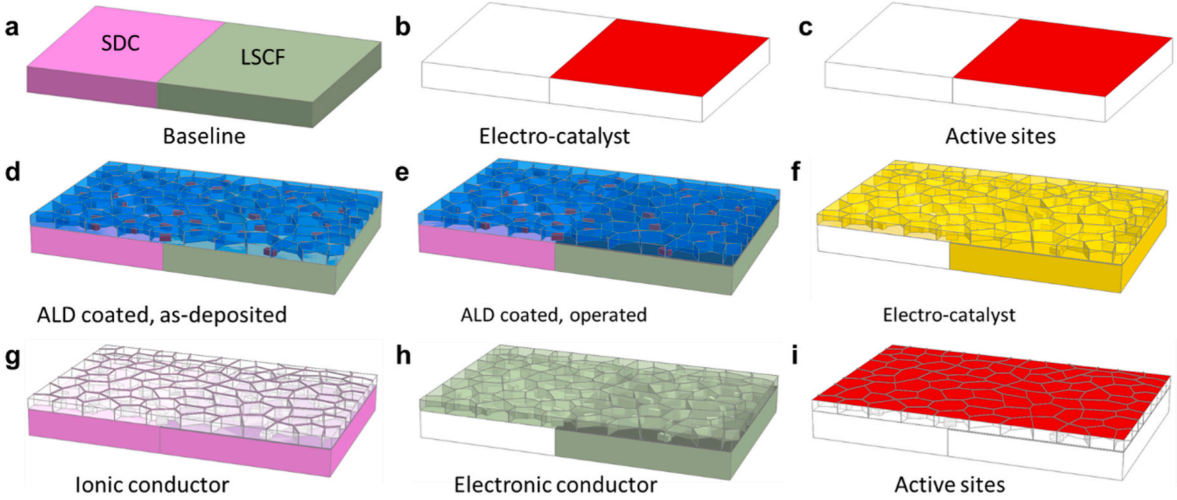

Fig. 6. Schematic of the surface architecture of the baseline cell no. 1 and cell no. 2 (or cell no. 4) LSCF cathode backbone with 8–10 nm Pt + CoO_x layer. **a.** Baseline LSCF phase, SDC phase and their phase boundary (interface). **b.** Electrocatalyst for baseline cell. **c.** Active ORR sites for baseline cell. **d.** Cell no. 2 cathode backbone with as-deposited conformal Pt + CoO_x layer. **e.** Surface layer after the electrochemical operation at 750 (or 650) °C. **f.** Distribution of electrocatalyst after the operation. **g.** Distribution of ionic conductor after the operation. **h.** Distribution of electrical conductor after the operation. **i.** Resultant cathode active ORR sites for cell with surface coating layer.

directions in terms of the fundamental design of the grain boundaries and strained critical interface for electrochemical reactions at elevated temperatures.

CRediT authorship contribution statement

Yun Chen: Conceptualization, Methodology, Investigation, Formal analysis, Data curation, Writing – original draft, Writing – review & editing. **Cesar O. Romo-De-La-Cruz:** Investigation, Methodology, Writing – review & editing. **Sergio A. Paredes-Navia:** Investigation, Formal analysis, Data curation. **Liang Liang:** Methodology, Investigation. **Alec Hinerman:** Investigation, Formal analysis, Data curation. **Jacky Prucz:** Conceptualization, Writing – review & editing, Supervision. **Mark Williams:** Conceptualization, Formal analysis, Writing – review & editing. **Xueyan Song:** Conceptualization, Methodology, Investigation, Formal analysis, Writing – original draft, Writing – review & editing, Data curation, Supervision, Project administration, Funding acquisition.

Declaration of competing interest

The authors declare that they have no known competing financial interests or personal relationships that could have appeared to influence the work reported in this paper.

Acknowledgment

X.S., Y.C., C.R., A.H., L.L., and S.P. acknowledges the financial support from DE-FE 0031251 and DE-FE0031665. X.S. acknowledges the support from NSF-DMR 1916581.

Appendix A. Supplementary data

Supplementary data to this article can be found online at https://doi.org/10.1016/j.jpowsour.2021.230715.

References

[1] A. Hauch, R. Küngas, P. Blennow, A.B. Hansen, J.B. Hansen, B.V. Mathiesen, M. B. Mogensen, Recent advances in solid oxide cell technology for electrolysis, Science 370 (2020) 6513.

[2] M. Mogensen, M. Chen, H. Frandsen, C. Graves, J. Hansen, K. Hansen, A. Hauch, T. Jacobsen, S. Jensen, T. Skafte, X. Sun, Reversible solid-oxide cells for clean and sustainable energy, Clean Energy 3 (3) (2019) 175–201.

[3] S.P. Jiang, Development of lanthanum strontium cobalt ferrite perovskite electrodes of solid oxide fuel cells – a review, Int. J. Hydrogen Energy 44 (14) (2019) 7448–7493.

[4] H. Okamoto, G. Kawamura, T. Kudo, Study of oxygen adsorption on platinum through observation of exchange current in a solid electrolyte concentration cell, Electrochim. Acta 28 (3) (1983) 379–382.

[5] H. Hu, M. Liu, Interfacial polarization characteristics of Pt|BaCe0.8Gd0.2O3|Pt Cells at Intermediate temperatures, J. Electrochem. *Soc.* 144 (10) (1997) 3561–3567.

[6] E. Schouler, G. Giroud, M. Kleitz, Applications selon Bauerle du tracé des diagrammes d'admittance complexe en électrochimie des solides, J. Chim. Phys. 70 (1973) 1309–1316.

[7] M.J. Verkerk, M.W.J. Hammink, A.J. Burggraaf, Oxygen transfer on substituted ZrO2, Bi2O3, and CeO2 electrolytes with platinum electrodes: I. Electrode resistance by D-C polarization, J. Electrochem. Soc. 130 (1) (1983) 70–78.

[8] R. Lewis, R. Gomer, Adsorption of oxygen on platinum, Surf. Sci. 12 (2) (1968) 157–176.

[9] J. Mizusaki, K. Amano, S. Yamauchi, K. Fueki, Electrode reaction at Pt, O2(g)/ stabilized zirconia interfaces. Part I: theoretical consideration of reaction model, Solid State Ionics 22 (4) (1987) 313–322.

[10] D. Ding, X. Li, S.Y. Lai, K. Gerdes, M. Liu, Enhancing SOFC cathode performance by surface modification through infiltration, Energy Environ. Sci. 7 (2) (2014) 552–575.

[11] J.T.S. Irvine, D. Neagu, M.C. Verbraeken, C. Chatzichristodoulou, C. Graves, M. B. Mogensen, Evolution of the electrochemical interface in high-temperature fuel cells and electrolysers, Nat. Energy 1 (1) (2016) 15014.

[12] J. Maier, Thermodynamics of nanosystems with a special view to charge carriers, Adv. Mater. 21 (25-26) (2009) 2571–2585.

[13] A.V. Chadwick, Transport in defective ionic materials: from bulk to nanocrystals, Phys. Status Solidi A 204 (3) (2007) 631–641.

[14] B.J. O'Neill, D.H. Jackson, J. Lee, C. Canlas, P.C. Stair, C.L. Marshall, J.W. Elam, T. F. Kuech, J.A. Dumesic, G.W. Huber, Catalyst design with atomic layer deposition, ACS Catal. 5 (3) (2015) 1804–1825.

[15] V. Sonn, A. Leonide, E. Ivers-Tiffée, Combined deconvolution and CNLS fitting approach applied on the impedance response of technical Ni/8YSZ cermet electrodes, J. Electrochem. Soc. 155 (7) (2008) B675.

[16] B. Liu, H. Muroyama, T. Matsui, K. Tomida, T. Kabata, K. Eguchi, Analysis of impedance spectra for segmented-in-series tubular solid oxide fuel cells, J. Electrochem. Soc. 157 (12) (2010) B1858.

[17] R. Barfod, M. Mogensen, T. Klemensø, A. Hagen, Y.-L. Liu, P. Vang Hendriksen, Detailed characterization of anode-supported SOFCs by impedance spectroscopy, J. Electrochem. Soc. 154 (4) (2007) B371.

[18] A. Leonide, B. Rüger, A. Weber, W.A. Meulenberg, E. Ivers-Tiffée, Impedance study of alternative (La,Sr)FeO3−δ and (La,Sr)(Co,Fe)O3−δ MIEC cathode compositions, J. Electrochem. Soc. 157 (2) (2010) B234.

[19] M. Kornely, A. Neumann, N.H. Menzler, A. Leonide, A. Weber, E. Ivers-Tiffée, Degradation of anode supported cell (ASC) performance by Cr-poisoning, J. Power Sources 196 (17) (2011) 7203–7208.

[20] A. Leonide, V. Sonn, A. Weber, E. Ivers-Tiffée, Evaluation and modeling of the cell resistance in anode-supported solid oxide fuel cells, J. Electrochem. Soc. 155 (1) (2008) B36.

[21] Y. Chen, Y. Choi, S. Yoo, Y. Ding, R. Yan, K. Pei, C. Qu, L. Zhang, I. Chang, B. Zhao, Y. Zhang, H. Chen, Y. Chen, C. Yang, B. deGlee, R. Murphy, J. Liu, M. Liu, A highly efficient multi-phase catalyst dramatically enhances the rate of oxygen reduction, Joule 2 (5) (2018) 938–949.

[22] S.B. Adler, Factors governing oxygen reduction in solid oxide fuel cell cathodes, Chem. Rev. 104 (10) (2004) 4791–4844.

[23] H. Yokokawa, T. Horita, N. Sakai, K. Yamaji, M.E. Brito, Y.P. Xiong, H. Kishimoto, Thermodynamic considerations on Cr poisoning in SOFC cathodes, Solid State Ionics 177 (35) (2006) 3193–3198.

[24] S.P. Jiang, X. Chen, Chromium deposition and poisoning of cathodes of solid oxide fuel cells – a review, Int. J. Hydrogen Energy 39 (1) (2014) 505–531.

[25] Y. Chen, Y. Fan, S. Lee, G. Hackett, H. Abernathy, K. Gerdes, X. Song, Interface and grain boundary degradation in LSM-YSZ composite Solid Oxide Fuel Cell cathodes operated in humidified air, J. Power Sources 438 (2019) 227043.

[26] Y. Chen, K. Gerdes, S.A. Paredes Navia, L. Liang, A. Hinerman, X. Song, Conformal electrocatalytic surface nanoionics for accelerating high-temperature electrochemical reactions in solid oxide fuel cells, Nano Lett. 19 (12) (2019) 8767–8773.

[27] J. Maier, Nano-ionics: more than just a fashionable slogan, J. Electroceram. 13 (1) (2004) 593–598.

[28] J.L.M. Rupp, A. Infortuna, L.J. Gauckler, Microstrain and self-limited grain growth in nanocrystalline ceria ceramics, Acta Mater. 54 (7) (2006) 1721–1730.

[29] H. Matsumoto, Y. Furuya, S. Okada, T. Tanji, T. Ishihara, Nanoionics phenomenon in proton-conducting oxide: effect of dispersion of nanosize platinum particles on electrical conduction properties, Sci. Technol. Adv. Mater. 8 (6) (2007) 531–535.

[30] R.I. Tomov, T.B. Mitchel-Williams, R. Maher, G. Kerherve, L. Cohen, D.J. Payne, R. V. Kumar, B.A. Glowacki, The synergistic effect of cobalt oxide and Gd-CeO2 dual infiltration in LSCF/CGO cathodes, J. Mater. Chem. A 6 (12) (2018) 5071–5081.

[31] W. Lee, H.J. Jung, M.H. Lee, Y.-B. Kim, J.S. Park, R. Sinclair, F.B. Prinz, Oxygen surface exchange at grain boundaries of oxide ion conductors, Adv. Funct. Mater. 22 (5) (2012) 965–971.

[32] A.M. Saranya, D. Pla, A. Morata, A. Cavallaro, J. Canales-Vázquez, J.A. Kilner, M. Burriel, A. Tarancón, Engineering mixed ionic electronic conduction in La0.8Sr0.2MnO3+δ nanostructures through fast grain boundary oxygen diffusivity, Adv. Energy Mater. 5 (11) (2015) 1500377.

[33] K.T. Lee, E.D. Wachsman, Role of nanostructures on SOFC performance at reduced temperatures, MRS Bull. 39 (9) (2014) 783–791.

[34] E. Navickas, T.M. Huber, Y. Chen, W. Hetaba, G. Holzlechner, G. Rupp, M. Stöger-Pollach, G. Friedbacher, H. Hutter, B. Yildiz, J. Fleig, Fast oxygen exchange and diffusion kinetics of grain boundaries in Sr-doped LaMnO3 thin films, Phys. Chem. Chem. Phys. 17 (12) (2015) 7659–7669.

[35] J.M. Polfus, B. Yildiz, H.L. Tuller, Origin of fast oxide ion diffusion along grain boundaries in Sr-doped LaMnO3, Phys. Chem. Chem. Phys. 20 (28) (2018) 19142–19150.

[36] F. Chiabrera, I. Garbayo, A. Tarancón, 17 - nanoionics and interfaces for energy and information technologies, in: N. Pryds, V. Esposito (Eds.), Metal Oxide-Based Thin Film Structures, Elsevier, 2018, pp. 409–439.

[37] F. Chiabrera, A. Morata, M. Pacios, A. Tarancón, Insights into the enhancement of oxygen mass transport properties of strontium-doped lanthanum manganite interface-dominated thin films, Solid State Ionics 299 (2017) 70–77.

[38] K. Develos-Bagarinao, H. Kishimoto, J. De Vero, K. Yamaji, T. Horita, Effect of La0.6Sr0.4Co0.2Fe0.8O3-δ microstructure on oxygen surface exchange kinetics, Solid State Ionics 288 (2016) 6–9.

[39] K. Develos-Bagarinao, H. Kishimoto, T. Ishiyama, T. Horita, H. Yokokawa, K. Yamaji, Invited, Probing oxide ion transport in fluorite and perovskite oxides for solid oxide fuel cells, ECS Trans. 72 (7) (2016) 139–148.

[40] Y. Chen, K. Gerdes, S.A. Paredes Navia, L. Liang, A. Hinerman, X. Song, Conformal electrocatalytic surface nanoionics for accelerating high-temperature electrochemical reactions in solid oxide fuel cells, Nano Lett. 19 (12) (2019) 8767–8773.

[41] F. Prado, T. Armstrong, A. Caneiro, A. Manthiram, Structural stability and oxygen permeation properties of Sr3−xLaxFe2−yCoyO7−δ (0≤x≤0.3 and 0≤y≤1.0), J. Electrochem. Soc. 148 (4) (2001) J7.

[42] C. Sowjanya, R. Mandal, S. Abhinay, A. Mohanta, S. Das, S.K. Pratihar, Effect of B-site substitution on the crystal structure, electrical conductivity and oxygen

transport properties of La0.5Sr0.5M0.2Fe0.8O3-δ (M = Co, Al, and Zn) perovskite, J. Solid State Chem. 285 (2020) 121237.
[43] J. Garcia-Barriocanal, A. Rivera-Calzada, M. Varela, Z. Sefrioui, E. Iborra, C. Leon, S.J. Pennycook, J. Santamaria, Colossal ionic conductivity at interfaces of epitaxial ZrO2:Y2O3/SrTiO3 heterostructures, Science 321 (2008) 5889, 676.
[44] A. Kushima, B. Yildiz, Oxygen ion diffusivity in strained yttria stabilized zirconia: where is the fastest strain? J. Mater. Chem. 20 (23) (2010) 4809–4819.
[45] J.L. MacManus-Driscoll, P. Zerrer, H. Wang, H. Yang, J. Yoon, A. Fouchet, R. Yu, M.G. Blamire, Q. Jia, Strain control and spontaneous phase ordering in vertical nanocomposite heteroepitaxial thin films, Nat. Mater. 7 (4) (2008) 314–320.
[46] J.R. Petrie, C. Mitra, H. Jeen, W.S. Choi, T.L. Meyer, F.A. Reboredo, J.W. Freeland, G. Eres, H.N. Lee, Strain control of oxygen vacancies in epitaxial strontium cobaltite films, Adv. Funct. Mater. 26 (10) (2016) 1564–1570.
[47] D. Lee, A. Grimaud, E.J. Crumlin, K. Mezghani, M.A. Habib, Z. Feng, W.T. Hong, M. D. Biegalski, H.M. Christen, Y. Shao-Horn, Strain influence on the oxygen electrocatalysis of the (100)-oriented epitaxial La2NiO4+δ thin films at elevated temperatures, J. Phys. Chem. C 117 (37) (2013) 18789–18795.
[48] K.A. Stoerzinger, W.S. Choi, H. Jeen, H.N. Lee, Y. Shao-Horn, Role of strain and conductivity in oxygen electrocatalysis on LaCoO3 thin films, J. Phys. Chem. Lett. 6 (3) (2015) 487–492.
[49] J.R. Petrie, H. Jeen, S.C. Barron, T.L. Meyer, H.N. Lee, Enhancing perovskite electrocatalysis through strain tuning of the oxygen deficiency, J. Am. Chem. Soc. 138 (23) (2016) 7252–7255.